Biallelic *TRIP13* mutations predispose to Wilms tumor and chromosome missegregation

Shawn Yost[1,13], Bas de Wolf[2,13], Sandra Hanks[1,13], Anna Zachariou[1], Chiara Marcozzi[3,4], Matthew Clarke[1], Richarda M de Voer[2,5], Banafsheh Etemad[2], Esther Uijttewaal[2], Emma Ramsay[1], Harriet Wylie[1], Anna Elliott[1], Susan Picton[6], Audrey Smith[7], Sarah Smithson[8], Sheila Seal[1], Elise Ruark[1] ⓘ, Gunnar Houge[9], Jonathon Pines[3,4], Geert J P L Kops[2,10,11,14] & Nazneen Rahman[1,12,14] ⓘ

Through exome sequencing, we identified six individuals with biallelic loss-of-function mutations in *TRIP13*. All six developed Wilms tumor. Constitutional mosaic aneuploidies, microcephaly, developmental delay and seizures, which are features of mosaic variegated aneuploidy (MVA) syndrome[1,2], were more variably present. Through functional studies, we show that *TRIP13*-mutant patient cells have no detectable TRIP13 and have substantial impairment of the spindle assembly checkpoint (SAC), leading to a high rate of chromosome missegregation. Accurate segregation, as well as SAC proficiency, is rescued by restoring TRIP13 function. Individuals with biallelic *TRIP13* or *BUB1B* mutations have a high risk of embryonal tumors[3], and here we show that their cells display severe SAC impairment. MVA due to biallelic *CEP57* mutations[4], or of unknown cause, is not associated with embryonal tumors and cells from these individuals show minimal SAC deficiency. These data provide insights into the complex relationships between aneuploidy and carcinogenesis.

Accurate chromosome segregation during cell division is required to maintain the correct number of chromosomes in cells. Errors of chromosome segregation can lead to aneuploidy, a term that describes cells with loss or gain of one or more chromosomes. Aneuploidy is an important cause of human disease and is implicated in diverse pathologies, including recurrent miscarriage, infertility, developmental disorders and cancer[5–7]. Many biological processes, including spindle assembly, chromatid–spindle attachment, attachment error correction and the SAC, are involved in ensuring that chromosome segregation proceeds flawlessly and that aneuploidy is prevented[6,8].

Rare individuals with constitutional mosaic aneuploidies involving varying chromosomes are well documented[1,2]. Affected individuals often have other clinical features such as microcephaly, developmental delay and various congenital abnormalities, and the term MVA is used to describe this condition[1–3]. Cancer predisposition is one of the most important associations of MVA, with affected individuals having substantially increased risk of childhood malignancies, particularly Wilms tumor and rhabdomyosarcoma[3,9,10].

We have been studying this rare condition for over a decade. We previously reported biallelic mutations in the (SAC) gene *BUB1B* as a cause of MVA and childhood cancer[3]. Thus far, we have identified 14 individuals with biallelic *BUB1B* mutations. More recently, we identified biallelic mutations in *CEP57*, which encodes a centrosomal protein, in four individuals with MVA, none of whom have developed cancer[4]. Together, these two genes only account for a proportion of MVA cases.

To identify additional MVA-related genes, we undertook exome sequencing in 43 individuals from 20 families, including 21 probands with MVA (**Supplementary Table 1**). We generated exome data using Illumina exome capture assays and called variants using the OpEx pipeline as previously described[11,12]. We performed two analyses to prioritize variants for further evaluation. We first undertook an individual proband analysis to identify genes with two rare variants, as MVA is a recessively inherited condition. We also identified genes with protein-truncating variants (PTVs) present in more than one proband, using the PTV prioritization method[4,12].

We identified a homozygous stop-gain mutation in the *TRIP13* gene (NM_004237), called *TRIP13* c.1060C>T_p.Arg354X, in three probands (ID_0319, ID_0644 and ID_7054) (**Table 1** and **Supplementary Fig. 1**). The mutation leads to nonsense-mediated mRNA decay (**Supplementary Fig. 2**) and the absence of detectable TRIP13 protein (**Supplementary Fig. 3**). Protein expressed from exogenous cDNA was present at a substantially lower level than wild-type TRIP13 (**Supplementary Fig. 4**). This shows that, in addition to altering mRNA stability, the mutation also directly affects the TRIP13 protein. Therefore, the *TRIP13* c.1060C>T_p.Arg354X allele is highly unlikely to produce any functional TRIP13 protein.

[1]Division of Genetics and Epidemiology, The Institute of Cancer Research, London, UK. [2]Hubrecht Institute–KNAW (Royal Netherlands Academy of Arts and Sciences), Utrecht, the Netherlands. [3]Division of Cancer Biology, The Institute of Cancer Research, London, UK. [4]Gurdon Institute and Department of Zoology, University of Cambridge, Cambridge, UK. [5]Department of Human Genetics, Radboud University Medical Center, Nijmegen, the Netherlands. [6]Children's and Adolescent Oncology and Haematology Unit, Leeds General Infirmary, Leeds, UK. [7]Yorkshire Regional Clinical Genetics Service, Chapel Allerton Hospital, Leeds, UK. [8]Clinical Genetics Service, St Michael's Hospital, Bristol, UK. [9]Center for Medical Genetics, Haukeland University Hospital, Bergen, Norway. [10]Cancer Genomics Netherlands, Utrecht, the Netherlands. [11]Center for Molecular Medicine, University Medical Center Utrecht, Utrecht, the Netherlands. [12]Cancer Genetics Unit, Royal Marsden NHS Foundation Trust, London, UK. [13]These authors contributed equally to this work. [14]These authors jointly directed this work. Correspondence should be addressed to N.R. (rahmanlab@icr.ac.uk) or G.J.P.L.K. (g.kops@hubrecht.eu).

Table 1 Summary of molecular and clinical findings in individuals with biallelic *TRIP13* mutations

ID	*TRIP13* mutations	Aneuploidy	Premature chromatid separation	Wilms tumor age at diagnosis	Current status	Other clinical features
ID_0319	c.1060C>T_p.Arg354X c.1060C>T_p.Arg354X	Yes	U	2 years	Alive, 6 years	Microcephaly, developmental delay, arthrogryposis
ID_0644	c.1060C>T_p.Arg354X c.1060C>T_p.Arg354X	Yes	Yes	4 years, relapse 5 years	Alive, 43 years	Growth retardation
ID_7054	c.1060C>T_p.Arg354X c.1060C>T_p.Arg354X	Yes	Yes	2 years	Alive, 5 years	Café-au-lait patches
ID_0649	c.1060C>T_p.Arg354X c.1060C>T_p.Arg354X	No	Yes	2 years, relapse 10 years	Died, 10 years	Microcephaly, growth retardation, seizures, abnormal skin pigmentation
ID_6112	c.1060C>T_p.Arg354X c.1060C>T_p.Arg354X	U	U	5 years	Alive, 6 years	
ID_7679	c.673-1G>C c.673-1G>C	No	U	1.3 years	Alive, 2.5 years	Microcephaly, seizures, developmental delay

Fuller details are provided in **Supplementary Figure 1**. U, unknown.

The three individuals had been independently recruited and there was no known relationship between them, but they were all from families of Asian origin. Interestingly, all three had Wilms tumor. To further explore the association of *TRIP13* with Wilms tumor, we performed exome sequencing in 11 UK individuals of reported Asian origin with Wilms tumor. Two, ID_0649 and ID_6112, were also homozygous for *TRIP13* c.1060C>T_p.Arg354X (**Table 1** and **Supplementary Fig. 1**). ID_0649 had been noted to have premature chromatid separation but no mosaic aneuploidies in lymphocytes. No constitutional karyotype has been performed in ID_6112, but the tumor karyotype was reported to be normal. Of note, the sister of ID_6112 died at 4 years of age after developing a Sertoli–Leydig cell tumor of the left ovary and acute myeloid leukemia (AML). No sample was available for mutation testing, but this observation suggests that biallelic *TRIP13* mutations may also predispose to cancers other than Wilms tumor.

The four available parental samples were all heterozygous for the mutation, consistent with recessive inheritance. The mutation was not present in the Exome Aggregation Consortium (ExAC) or ICR1000 series[13,14], nor was it present in 11,677 other exomes we have analyzed with the same pipeline. Multidimensional scaling analysis strongly suggested that the families originated from Pakistan (**Supplementary Fig. 5**). Exploration of the available family history suggests that the families come from the Azad Kashmir region of Pakistan. Many Azad Kashmir families were given work permits for the UK in the 1960s because of the construction of the Mangla Dam, which led to large-scale local displacement. Further evaluation of the contribution of the *TRIP13* mutation to Wilms tumor in this population would therefore be of interest.

We subsequently became aware of a Norwegian girl, ID_7679, who developed Wilms tumor at 15 months, who was homozygous for a different truncating *TRIP13* mutation. The mutation, c.673-1G>C, is predicted to disrupt the canonical 3′ splice site in intron 7 of *TRIP13*, and a new splice site 2 bp upstream is predicted to be used, resulting in a 2-bp frameshift and premature protein truncation. No constitutional mosaic aneuploidies were observed in her lymphocytes.

These data provide compelling genetic evidence that *TRIP13* is a cancer predisposition gene. Biallelic loss-of-function *TRIP13* mutations confer a high risk of Wilms tumor and also predispose to chromosome segregation dysfunction, which can manifest as mosaic aneuploidies and/or premature chromatid separation. There were no consistent phenotypic features among the six probands, although developmental delay, microcephaly, seizures and growth retardation were each noted in more than one individual (**Table 1** and **Supplementary Fig. 1**).

TRIP13 encodes a highly conserved AAA+ATPase that contributes to homolog pairing, synapsis and recombination during meiosis[15].

In mitosis, TRIP13 remodels the crucial SAC effector MAD2 from a 'closed' (active) to an 'open' (inactive) form[16,17]. This has a dual impact on SAC function: in prometaphase, MAD2 remodeling is thought to
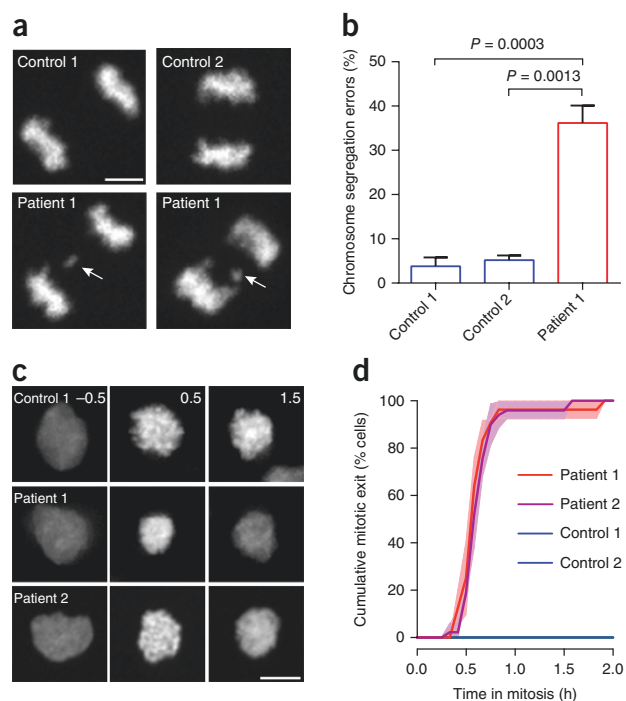

Figure 1 *TRIP13* loss-of-function mutations cause chromosome segregation errors and SAC deficiency. (**a**) Representative anaphases of immortalized control (top) and *TRIP13*-mutant patient (bottom) lymphoblasts expressing H2B-mNeon, showing a lagging chromosome in the bottom panels (white arrows). Scale bar, 5 μm. (**b**) Quantification of the chromosome segregation errors of lymphoblasts as visualized in **a**. Each bar depicts the mean of three (control 2) or four (control 1 and patient 1) independent experiments ± s.e.m., with 160 (control 1), 93 (control 2) and 64 (patient 1) cells in total. *P* values ≤ 0.05 from two-sided unpaired Student's *t* tests are shown. Cells from patient 1 show increased levels of chromosome segregation errors. (**c**) Representative images of H2B-mNeon-expressing control (top) and patient (bottom) lymphoblasts going through mitosis (time in hours with mitotic entry at *t* = 0.0) in the presence of nocodazole. Unlike control cell lines, both patient cell lines had exited from mitosis by 1.5 h (third column of the second and third rows). Scale bar, 10 μm. (**d**) Analysis of the mitotic delay of cells as visualized in **c**, indicating the cumulative percentage of cells that exited from mitosis as a function of time (mean of three independent experiments ± s.e.m. (shaded regions)), with 30 (controls 1 and 2) or 90 (patients 1 and 2) cells in total. Both patient cell lines escaped mitotic arrest within 1 h. Patient 1, ID_0644; patient 2, ID_7054.
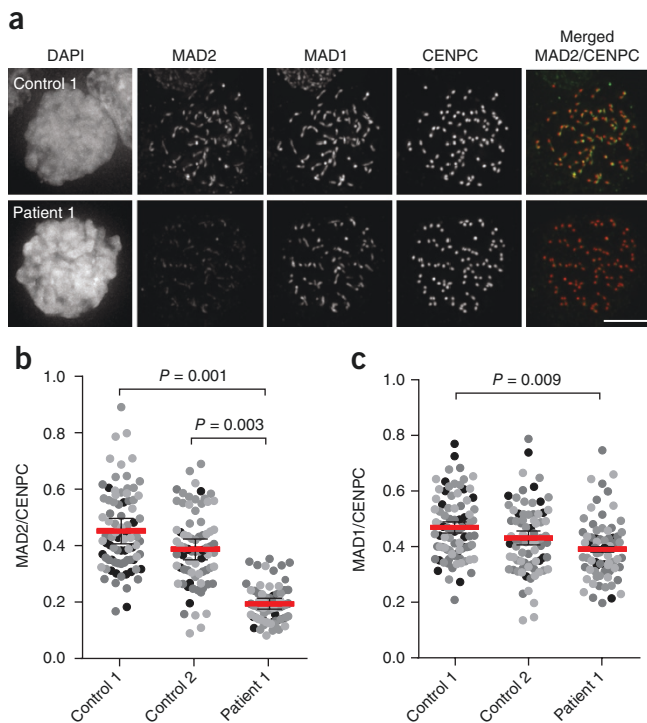
Figure 2 *TRIP13* loss-of-function mutations cause reduced levels of MAD2 on unattached kinetochores. (**a–c**) Immunofluorescence labeling (**a**) and quantification (**b,c**) of the indicated proteins in nocodazole-arrested control or patient lymphoblasts. In the plots, each dot represents one cell, with dots from separate independent experiments in different shades of gray. The red bar depicts the mean of four experiments ± s.e.m., with 82 (control 1), 75 (control 2) and 71 (patient 1) cells in total. *P* values ≤ 0.05 from two-sided unpaired Student's *t* tests are shown. Cells from patient 1 had reduced kinetochore levels of MAD2, but not MAD1, in comparison to the controls. Patient 1, ID_0644; CENPC, kinetochore marker; DAPI, DNA stain. Scale bar, 3 μm.

Figure 3 SAC deficiency and CIN caused by *TRIP13* loss of function is rescued with wild-type but not mutant TRIP13. (**a**) Quantification of the chromosome segregation errors of *TRIP13*-mutated patient lymphoblasts expressing H2B-mNeon or coexpressing GFP-tagged wild-type TRIP13 (GFP-TRIP13 wt). Each bar depicts the mean of three (patient 1) or four (patient 1 + TRIP13 wt) independent experiments ± s.e.m., with 88 (patient 1) and 92 (patient 1 + TRIP13 wt) cells in total. *P* values ≤ 0.05 from two-sided unpaired Student's *t* tests are shown. Addition of GFP-TRIP13 wt to cells from patient 1 significantly reduced the rate of chromosome missegregation. (**b**) Analysis of mitotic delay as in **Figure 1d** in nocodazole-treated patient lymphoblasts expressing H2B-mNeon or coexpressing GFP-TRIP13 wt. The mean of three independent experiments ± s.e.m. (shaded regions) is shown, with 100 (patient 1) and 35 (patient 1 + TRIP13 wt) cells in total. Cells from patient 1 expressing GFP-TRIP13 wt now maintained mitotic arrest. (**c**) Analysis of mitotic delay as in **b** in nocodazole-treated wild-type or *TRIP13*-knockout (KO) HCT116 cells expressing H2B-mNeon, coexpressing GFP-TRIP13 wt or coexpressing TRIP13 Arg354X. The mean of three independent experiments ± s.e.m. (shaded regions) is shown, with 85 (HCT116 wt), 90 (*TRIP13* KO and *TRIP13* KO + TRIP13 wt) and 48 (*TRIP13* KO + TRIP13 Arg354X) cells in total. HCT116 wt and *TRIP13* KO + TRIP13 wt cells both maintained mitotic arrest, unlike *TRIP13* KO and *TRIP13* KO + TRIP13 Arg354X cells. Patient 1, ID_0644.

enable continuous replenishment of the MAD2 pools that can be activated by unattached kinetochores for the generation of the initial SAC inhibitor. TRIP13 thus ensures robust and long-lasting SAC signaling. In metaphase, however, when no new active MAD2 is generated by kinetochores, MAD2 inactivation by TRIP13 promotes disassembly of the inhibitor and causes SAC silencing and mitotic exit[18–20].

We sought to examine which defective molecular processes underlie aneuploidy and chromosome missegregation in *TRIP13*-mutant patients. We first infected immortalized *TRIP13*-mutant patient lymphoblasts with virus encoding histone H2B (H2B)-mNeon to visualize chromatin. Live-cell imaging showed that patient lymphoblasts had high levels of chromosome segregation errors, such as lagging chromosomes and chromosome bridges (**Fig. 1a,b**). To understand how *TRIP13* mutations cause chromosomal instability (CIN) in patient cells, we examined the fidelity of the SAC, the main chromosome segregation surveillance mechanism in which TRIP13 has been implicated. To this end, we analyzed cells for their ability to maintain mitotic arrest after exposure to the spindle poison nocodazole (**Fig. 1c** and **Supplementary Fig. 6**). Control cells maintained the arrest for >2 h, whereas all cells from two different *TRIP13*-mutant patients escaped the arrest within 1 h (**Fig. 1c,d**). Mitotic exit despite unattached chromosomes is indicative of a compromised SAC.

To gain insight into the molecular defect causing SAC impairment, we analyzed SAC protein expression and subcellular localization.
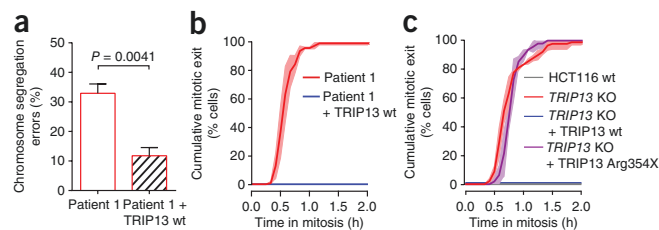
Immunofluorescence imaging of the SAC effector MAD2 in nocodazole-treated cells showed that *TRIP13*-mutant patient cells recruited ~50% fewer molecules of MAD2 to their unattached kinetochores (**Fig. 2a,b**). Kinetochore levels of the MAD2 receptor MAD1 were unaffected (**Fig. 2c**). Absence of TRIP13 caused increased overall p31[comet] expression in one patient and reduced overall MAD2 expression in both patients (**Supplementary Fig. 7**), consistent with data reported in *TRIP13*-knockout HeLa cells[20].

We next restored TRIP13 function by expressing GFP-TRIP13 in patient lymphoblasts using lentiviral delivery. Notably, GFP-TRIP13 expression rescued the CIN as well as the SAC defect (**Fig. 3a,b**). Moreover, GFP-tagged Arg354X TRIP13 was unable to rescue an impaired SAC caused by CRISPR–Cas9-mediated knockout of the *TRIP13* gene in HCT116 chromosomally stable colorectal carcinoma cells (**Fig. 3c** and **Supplementary Figs. 8** and **9**). These observations provide an explanation for the chromosome segregation defects observed in individuals with biallelic *TRIP13* loss-of-function mutations. They also show that the SAC defects and resulting CIN are directly due to the loss of TRIP13 function caused by the homozygous *TRIP13* c.1060C>T_p.Arg354X mutations.

TRIP13 and BUBR1 (the protein encoded by *BUB1B*) are close functional partners in the SAC[15]. BUBR1 is part of the anaphase inhibitory complex MCC, which also includes MAD2, the main target of TRIP13's remodeling activity in mitosis[21]. Notably, severe SAC impairment was observed in *TRIP13*-mutant and *BUB1B*-mutant patient cells but not in cells from patients with *CEP57* mutations or in whom the cause of MVA remains unclear after exome sequencing (**Fig. 4**).

All six children with biallelic *TRIP13* mutations developed Wilms tumor in childhood, five of whom were successfully treated (**Table 1**). Limited information is available, but there were no obvious distinctive histopathological features in the tumors. Individuals with biallelic *BUB1B*
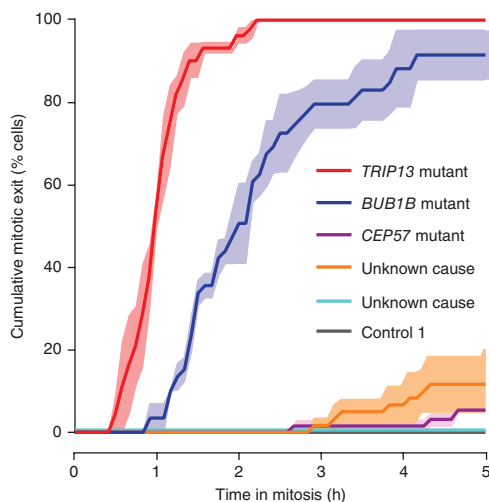
Figure 4 Patient cells with *TRIP13* or *BUB1B* mutations have a severely compromised SAC. Analysis of mitotic delay as in **Figure 1d** in nocodazole-treated patient lymphoblasts from patients with MVA treated with far-red DNA dye to visualize the DNA, showing the cumulative percentage of cells that exited from mitosis as a function of time (mean of three independent experiments ± s.e.m. (shaded regions), with 60 cells in total per cell line. Only *TRIP13*-mutant and *BUB1B*-mutant patient cells rapidly escaped from mitotic arrest.

mutations are also at high risk of childhood embryonal tumors. In fact, all MVA cases with childhood solid tumors in our series had either *BUB1B* or *TRIP13* mutations. By contrast, only one individual with MVA in our series without mutations in *BUB1B* or *TRIP13* had developed cancer, an acute lymphoblastic leukemia (ALL), at 3 years; the cause of MVA remains unknown in this child[10]. It is therefore tempting to speculate that the high cancer risk may be causally related to severe impairment of the SAC. Irrespective of the mechanism, our findings have clinical utility, indicating that individuals positive for mutations in *BUB1B* and *TRIP13* are at high risk of cancer and require close surveillance, whereas other individuals with MVA may be at lower cancer risk.

The data also suggest that the mechanism generating aneuploidy in affected individuals determines the cancer risk, not the aneuploidy per se. If confirmed, this is an important distinction, as there has long been a debate regarding whether aneuploidy is a cause or consequence of cancer[5]. Further studies into the biological sequelae of these rare human mutations may therefore provide insights into the complex relationships between aneuploidy and carcinogenesis.

URLs. OpEx variant calling pipeline, http://www.icr.ac.uk/opex; ICR1000 UK exome series, http://www.icr.ac.uk/icr1000exomes; Exome Aggregation Consortium (ExAC), http://exac.broadinstitute.org/; 1000 Genomes Project, http://www.internationalgenome.org/; PLINK, http://pngu.mgh.harvard.edu/~purcell/plink/; Exon-Primer from UCSC Genome Browser, http://genome.ucsc.edu/.

METHODS

Methods, including statements of data availability and any associated accession codes and references, are available in the online version of the paper.

Note: Any Supplementary Information and Source Data files are available in the online version of the paper.

AUTHOR CONTRIBUTIONS
N.R. designed and oversaw the study. G.J.P.L.K. designed and oversaw the functional experiments. E. Ramsay undertook the exome sequencing. S.H., H.W. and S. Seal performed the molecular analyses. S.Y., M.C. and E. Ruark performed bioinformatic analyses. B.d.W., E.U., R.M.d.V., B.E. and C.M. undertook functional analyses under the supervision of G.J.P.L.K., and J.P., S.P., A.S., S. Smithson and G.H. provided samples and data, coordinated by A.Z. and A.E. S.Y., S.H., B.d.W., A.Z., G.J.P.L.K. and N.R. wrote the manuscript with input from the other authors.

1. García-Castillo, H., Vásquez-Velásquez, A.I., Rivera, H. & Barros-Núñez, P. Clinical and genetic heterogeneity in patients with mosaic variegated aneuploidy: delineation of clinical subtypes. *Am. J. Med. Genet. A.* **146A**, 1687–1695 (2008).
2. Warburton, D., Anyane-Yeboa, K., Taterka, P., Yu, C.Y. & Olsen, D. Mosaic variegated aneuploidy with microcephaly: a new human mitotic mutant? *Ann. Genet.* **34**, 287–292 (1991).
3. Hanks, S. *et al.* Constitutional aneuploidy and cancer predisposition caused by biallelic mutations in *BUB1B*. *Nat. Genet.* **36**, 1159–1161 (2004).
4. Snape, K. *et al.* Mutations in *CEP57* cause mosaic variegated aneuploidy syndrome. *Nat. Genet.* **43**, 527–529 (2011).
5. Ricke, R.M. & van Deursen, J.M. Aneuploidy in health, disease, and aging. *J. Cell Biol.* **201**, 11–21 (2013).
6. Holland, A.J. & Cleveland, D.W. Boveri revisited: chromosomal instability, aneuploidy and tumorigenesis. *Nat. Rev. Mol. Cell Biol.* **10**, 478–487 (2009).
7. Torres, E.M., Williams, B.R. & Amon, A. Aneuploidy: cells losing their balance. *Genetics* **179**, 737–746 (2008).
8. Thompson, S.L., Bakhoum, S.F. & Compton, D.A. Mechanisms of chromosomal instability. *Curr. Biol.* **20**, R285–R295 (2010).
9. Kajii, T. *et al.* Cancer-prone syndrome of mosaic variegated aneuploidy and total premature chromatid separation: report of five infants. *Am. J. Med. Genet.* **104**, 57–64 (2001).
10. Jacquemont, S., Bocéno, M., Rival, J.M., Méchinaud, F. & David, A. High risk of malignancy in mosaic variegated aneuploidy syndrome. *Am. J. Med. Genet.* **109**, 17–21, discussion 16 (2002).
11. Ruark, E. *et al.* OpEx—a validated, automated pipeline optimised for clinical exome sequence analysis. *Sci. Rep.* **6**, 31029 (2016).
12. Mahamdallie, S.S. *et al.* Mutations in the transcriptional repressor *REST* predispose to Wilms tumor. *Nat. Genet.* **47**, 1471–1474 (2015).
13. Lek, M. *et al.* Analysis of protein-coding genetic variation in 60,706 humans. *Nature* **536**, 285–291 (2016).
14. Ruark, E. *et al.* The ICR1000 UK exome series: a resource of gene variation in an outbred population. *F1000Res* **4**, 883 (2015).
15. Vader, G. Pch2^{TRIP13}: controlling cell division through regulation of HORMA domains. *Chromosoma* **124**, 333–339 (2015).
16. Eytan, E. *et al.* Disassembly of mitotic checkpoint complexes by the joint action of the AAA-ATPase TRIP13 and p31^{comet}. *Proc. Natl. Acad. Sci. USA* **111**, 12019–12024 (2014).
17. Ye, Q. *et al.* TRIP13 is a protein-remodeling AAA$^+$ ATPase that catalyzes MAD2 conformation switching. *eLife* **4**, e07367 (2015).
18. Wang, K. *et al.* Thyroid hormone receptor interacting protein 13 (TRIP13) AAA-ATPase is a novel mitotic checkpoint–silencing protein. *J. Biol. Chem.* **289**, 23928–23937 (2014).
19. Nelson, C.R., Hwang, T., Chen, P.H. & Bhalla, N. TRIP13PCH-2 promotes Mad2 localization to unattached kinetochores in the spindle checkpoint response. *J. Cell Biol.* **211**, 503–516 (2015).
20. Ma, H.T. & Poon, R.Y. TRIP13 regulates both the activation and inactivation of the spindle-assembly checkpoint. *Cell Rep.* **14**, 1086–1099 (2016).
21. Vleugel, M., Hoogendoorn, E., Snel, B. & Kops, G.J. Evolution and function of the mitotic checkpoint. *Dev. Cell* **23**, 239–250 (2012).

ONLINE METHODS

Samples. The study was approved by the London Multicentre Research Ethics Committee (05/MRE02/17). For mutational analyses, DNA was obtained through our ongoing research of cancer predisposition syndromes. Appropriate consent was obtained from patients and/or parents, as applicable. DNA was extracted from whole blood or an Epstein–Barr virus (EBV)-transformed lymphoblastoid cell line (ID_0644, ECACC ID: 96061307) using standard protocols.

For the functional experiments, the following patient LCLs were used: ID_0644 (patient 1, biallelic *TRIP13* mutations, ECACC ID: 96061307), ID_7054 (patient 2, biallelic *TRIP13* mutations), ID_0675 (patient with biallelic *BUB1B* mutations, Coriell ID: GM22006), ID_0663 (patient with biallelic *CEP57* mutations, Coriell ID: GM21654), ID_0639 (Coriell ID: GM09703) and ID_5728_01 (ECACC ID: FACT5728DLB).

Two control LCLs were also used: ID_5728_03, an unaffected sibling of ID_5728_01 (control 1, ECACC ID: FACT5728KC), and C0106 (control 2, ECACC ID: 91071212). Cells were cultured in RPMI supplemented with 15% FBS, 100 µg/ml penicillin-streptomycin and 2 mM alanyl-glutamine. Cells expressing H2B-mNeon were created by lentiviral transduction, using standard procedures.

Exome sequencing. We performed exome sequencing using the TruSeq Exome Enrichment kit (Illumina) or the Nextera Rapid Capture Exome kit (Illumina). For TruSeq exome sequencing, we prepared libraries from 1.5 µg of genomic DNA using the TruSeq Paired-End DNA Sample Preparation kit (Illumina). DNA was fragmented using Covaris technology, and libraries were prepared without gel size selection. For Nextera exome sequencing, we prepared libraries from 50 ng of genomic DNA using the Nextera DNA Sample Preparation kit (Illumina). Captured DNA libraries were PCR amplified using the supplied paired-end PCR primers. Paired-end sequencing was performed on an Illumina HiSeq 2000 or HiSeq 2500 (high-output mode) using v3 chemistry.

Alignment and variant calling. We used the OpEx v1.0 pipeline to perform variant calling (http://www.icr.ac.uk/opex)[11]. Raw data were converted to FASTQ files using CASAVA version 1.8.2 with default settings. The OpEx v1.0 pipeline uses Stampy[22] to map to the human reference genome, Picard (http://picard.sourceforge.net/) to flag duplicates, Platypus[23] to call variants and CAVA[24] to provide consistent annotation of variants with the HGVS-compliant CSN (Clinical Sequencing Notation) standard v1.0 (ref. 24). Only high-quality calls, as defined by OpEx, were used in the analyses.

Reference data sets. We used the following data sets as control samples: ExAC data[13] version 3 accessed on 13 November 2015 (excluding the TCGA samples), the 1000 Genomes Project data[25] and the ICR1000 UK exome series[14]. The ICR1000 UK exome series was generated using the same sequencing and analysis pipelines as the cases.

PTV prioritization method. The PTV prioritization method is a gene-based strategy that aims to prioritize potential disease-associated genes for follow-up by leveraging two properties of PTVs: (i) the strong association of rare truncating variants with disease and (ii) collapsibility; different PTVs within a gene typically result in the same functional effect and can be combined equally. We output all the predicted PTVs: stop gains, coding frameshifts and essential splice-site variants (−2, −1, +1, +2). For this experiment, we defined 'rare' as PTVs that had an alternate allele frequency <1% in the control data sets. We next stratified the genes according to the number of different rare PTVs called in each affected individual.

Recessive analysis. We prioritized variants for evaluation in each affected individual assuming a recessive inheritance model. We removed all intronic, 3′ and 5′ UTR, and non-essential splice-site variants and any variant that had an allele frequency >1% in control data sets. We also removed any heterozygous variant combination pair or homozygous alternate variant in which both alleles were from a single parent.

Sanger sequencing. We used Sanger sequencing to confirm the *TRIP13* mutations identified in patients by exome sequencing and to confirm the presence of

mutation following CRISPR–Cas9-mediated knockout of *TRIP13* in HCT116 cells. For patient samples, primers were designed using Exon-Primer from the UCSC Genome Browser. PCRs were prepared using the Qiagen Multiplex PCR kit according to the manufacturer's instructions. Amplicons were bidirectionally sequenced using the BigDye Terminator Cycle sequencing kit and an ABI 3730 automated sequencer (Life Technologies). We analyzed sequencing traces using Mutation Surveyor software (SoftGenetics) and by visual inspection. For samples derived from HCT116 cells, primers were designed manually and PCRs were prepared using the Phusion High-Fidelity DNA Polymerase PCR protocol (New England BioLabs) according to the manufacturer's instructions. Amplicons were sent to Macrogen for sequencing, and sequencing traces were analyzed using ApE version v2.0.49.10 software and by visual inspection. Primer sequences are available upon request.

Multidimensional scaling analysis. We used the multidimensional scaling (MDS) analysis tool provided by PLINK to identify which population in the 1000 Genomes Project was most similar to the individuals with the *TRIP13* c.1060C>T_p.Arg354X mutation. To identify the set of variants to use in the MDS analysis, we took the union of all coding and splice-site base substitutions in the 43 individuals with exome sequencing data and the 1000 Genomes Project individuals. We then removed variants for which 20 or more individuals had less than 15× coverage. We selected a subset of the individuals to use in the MDS analysis (**Supplementary Fig. 5**). We then used PLINK to remove variants with a minor allele frequency <0.01 or a Hardy–Weinberg equilibrium P value $<1 \times 10^{-10}$. We removed non-independent variants using default settings for the --indep-pairwise method in PLINK (--indep-pairwise 50 5 0.5). We then used the MDS algorithm (--mds-plot) to extract the first four dimensions from the variant data.

HCT116 cell culture and *TRIP13* knockout. HCT116 cells, obtained from ATCC and tested negative for mycoplasma, were cultured in McCoy's-5A medium supplemented with 10% Tet-approved FBS, 100 µg/ml penicillin-streptomycin and 2 mM alanyl-glutamine. HCT116 *TRIP13*-knockout cells were generated by transient expression of pSpCas9(BB)-2A-GFP (Addgene, 48138) with single-guide RNA (sgRNA) against exon 11 (sgTRIP13 in **Supplementary Table 2**), followed by single-cell FACS sorting of GFP+ cells. Knockouts were verified by immunoblotting for protein expression and Sanger sequencing (**Supplementary Figs. 8** and **9**).

HeLa cell culture and stable Trex Flp-In cell line creation. HeLa Trex Flp-In cells (a gift from S. Taylor, University of Manchester) were grown in high-glucose DMEM supplemented with 10% Tet-approved FBS, 100 µg/ml penicillin-streptomycin, 2 mM alanyl-glutamine, 4 µg/ml blasticidin and 200 µg/ml hygromycin. To generate stably integrated HeLa Flp-In cell lines, pcDNA5 constructs were cotransfected with pOG44 recombinase in a 1:9 ratio using FuGENE HD (Roche) according to the manufacturer's instructions. Constructs were expressed by addition of 1 µg/ml doxycycline for 24 h.

Plasmids, cloning and virus production. For the HeLa Trex Flp-In cell lines stably expressing *TRIP13*, pcDNA5-LAP-TRIP13-WT was created by cloning *TRIP13* cDNA derived from HeLa cells into empty pcDNA5-LAP using the cDNA PCR primers listed in **Supplementary Table 2** and digestion with BamHI and SpeI. pcDNA5-LAP-TRIP13-p.Arg354X was created by PCR mutagenesis of pcDNA5-LAP-TRIP13-WT using the Gibson Assembly strategy[26] with two fragments generated using the Mutagenesis 1 and 2 PCR primers listed in **Supplementary Table 2**.

Lentiviral *TRIP13* constructs were derived from a lentiviral construct encoding fluorescently tagged H2B and a puromycin resistance cassette (pLV-H2B-mNeon-IRES-Puro)[27]. The fluorescently tagged H2B was substituted by LAP-TRIP13-WT derived from pcDNA5-LAP-TRIP13-WT (see above) using the LAP-TRIP13-WT PCR primers listed in **Supplementary Table 2** and digestion with AscI and NheI. For the subsequent steps, the Gibson Assembly strategy was used[26]. The puromycin resistance cassette was substituted by fluorescently tagged H2B (H2B-mNeon 1 and 2 primers listed in **Supplementary Table 2**). The CMV promoter was substituted by the ubiquitin promoter from the pUB6/V5-His vector (Invitrogen) (pUB 1 and 2 primers listed in **Supplementary Table 2**). Finally, the *TRIP13* c.1060C>T_p.Arg354X

mutation was inserted by assembling two PCR fragments generated with the Mutagenesis 1 and 2 primers listed in **Supplementary Table 2**.

Virions were generated by transient transfection of HEK 293T cells with the transfer vector and separate plasmids that express Gag-Pol, Rev, Tat and VSV-G. Supernatants were clarified by filtration.

Live-cell imaging analysis of chromosome segregation errors. Lymphoblasts stably expressing H2B-mNeon were arrested in early S phase for 24 h by the addition of 2 mM thymidine. Cells were then released from thymidine for 4 h and mitotic progression was assayed. Cells were plated in eight-well Ibidi μ-slides in a thin layer of 0.15% UltraPure agarose with a layer of 0.3% agar on top. Cells were imaged in a heated chamber (37 °C and 5% CO_2). Images were acquired every 3 min at 1 × 1 binning in 15 × 1.5 μm z layers and projected to a single layer by maximum-intensity projection using NIS-Elements software 4.45.

Imaging was performed with a Nikon Ti-Eclipse microscope equipped with a CSUW spinning disk (Yokogawa), a Borealis Andor iXon Ultra 888 EMCCD camera, a 40× water objective with N.A. 1.15 and W.D. 0.6 mm, and a 488-nm laser. Analysis of these experiments was carried out with ImageJ software. Chromosome segregation errors include one or more lagging chromosomes, misaligned chromosomes, chromosome bridges and multipolar mitoses. The percentage of chromosome segregation errors is the amount of divisions with one or more mitotic errors divided by the total amount of divisions. Three or four independent experiments were performed. Quantifications were subjected to two-sided unpaired Student's t tests.

Live-cell imaging analysis of mitotic delay. Lymphoblasts or HCT116 cells were synchronized and plated as described above (HCT116 cells were plated in 24-well plates without agarose). After release from thymidine, mitotic progression was assayed in the presence of 0.83 μM nocodazole. For the experiments in **Figure 4**, lymphoblasts were incubated with 100 nM SiR-DNA dye (Spirochrome) for 4 h before imaging, to facilitate visualization of mitotic arrest. For the experiments in **Figure 3**, cells were infected with a lentivirus expressing LAP-TRIP13 (WT or p.Arg354X)-IRES-H2B-mNeon, ensuring that H2B-mNeon-positive cells coexpressed LAP-TRIP13.

Images (far red for **Fig. 4**; mNeon for **Figs. 1d** and **3b,c**) were acquired every 5 min on a Nikon Ti-Eclipse wide-field microscope equipped with an Andor Zyla 4.2 sCMOS camera, a 40× oil objective with N.A. 1.3 and W.D. 0.2 mm, and a Lumencor SpectraX light engine. Analysis of these experiments was carried out with ImageJ software. Time in mitosis was defined as the time between chromosome condensation and anaphase onset. Three independent experiments were performed. Quantifications were subjected to two-sided unpaired Student's t tests.

Immunofluorescence imaging. Cells were plated on round 12-mm coverslips (coated with poly-L-lysine (Santa Cruz) according to the manufacturer's instructions for LCLs) and treated for 2.5 h with 3.3 μM nocodazole and 5 μM MG132 before being pre-extracted with 0.1% Triton X-100 in PEM (100 mM PIPES pH 6.8, 1 mM $MgCl_2$ and 5 mM EGTA) for 55–65 s before fixation with zinc formalin fixative, 1:1 in PEM with 0.1% Triton X-100, for 5–10 min. Coverslips were washed twice with cold PBS and blocked with 3% BSA in PBS for 16 h at 4 °C, incubated with primary antibodies for 16 h at 4 °C, washed four times with PBS containing 0.1% Triton X-100 and incubated with secondary antibodies for 1 h at room temperature. Coverslips were then washed four times with 0.1% Triton X-100 in PBS and mounted using ProLong Gold Antifade with DAPI (Molecular Probes). All images were acquired on a deconvolution system (DeltaVision Elite, Applied Precision/GE Healthcare) equipped with a 100×/1.40 N.A. UPlanSApo objective (Olympus) using SoftWorx 6.0 software (Applied Precision/GE Healthcare). Images are maximum-intensity projections of deconvolved stacks. A CellProfiler40 (ref. 28) pipeline was followed to threshold and select all kinetochores and all chromosome areas (excluding kinetochores) using DAPI and CENPC. This was used to calculate the relative average kinetochore intensity of various proteins ((kinetochores − chromosome arm intensity (kinetochore-localized protein of interest))/(kinetochores − chromosome arm intensity (CENPC))). Quantifications were subjected to two-sided unpaired Student's t tests. The primary antibodies used were guinea pig anti-CENPC (MBL International, PD030), rabbit anti-MAD2 (custom raised against full-length 6×His-tagged MAD2 as the antigen) and mouse anti-MAD1 (Millipore, MABE867). The secondary antibodies used were goat anti–guinea pig Alexa Fluor 647 (A21450), goat anti-rabbit Alexa Fluor 488 (A11034) and goat anti-mouse Alexa Fluor 568 (A11031), all obtained from Invitrogen Molecular Probes.

qRT–PCR. Lymphoblasts were seeded at 500,000 cells/ml in 20 ml of medium and split in two the following day. 50% of cells were treated with 100 μg/ml cycloheximide (Sigma) for 4.5 h, and the remaining cells were left untreated. Total mRNA was extracted using the RNeasy Mini kit (Qiagen). Equal amounts of RNA (0.5 μg) were reverse transcribed using the iScript cDNA Synthesis kit (Bio-Rad) with an optimum blend of oligo(dT) and random hexamers. Real-time quantification was performed with IQ SYBR Green Supermix (Bio-Rad) on a CFX Connect Real-Time system (Bio-Rad) using probes generated against *TRIP13* and *GAPDH* (qPCR 1 and 2 primer pairs listed in **Supplementary Table 2**). The data were normalized to *GAPDH* expression and patient sample data were compared to the average expression of two control samples to quantify relative expression levels of *TRIP13*, using the $2^{-\Delta\Delta C_T}$ method. Three independent experiments were performed.

Immunoblotting analysis of TRIP13 expression. For the data shown in **Supplementary Figures 3**, **4** and **7**, cells were treated as indicated and lysed in Laemmli lysis buffer (4% SDS, 120 mM Tris pH 6.8 and 20% glycerol). Lysates were processed for SDS–PAGE and transferred to nitrocellulose membranes. Immunoblotting was performed using standard protocols. Visualization of signals was performed on an Amersham Imager 600 scanner using enhanced chemiluminescence. For quantification of immunostaining, all images of similarly stained independent experiments were acquired with identical illumination settings. The primary antibodies used were mouse anti-tubulin (Sigma, T5168), mouse anti-GFP (Roche, 11-814-460-001), rabbit anti–histone H3 (Abcam, ab1791) and rabbit anti-TRIP13 (Abcam, ab128171). The secondary antibodies used were goat anti-mouse HRP (170-6516) and goat anti-rabbit HRP (170-6515), both obtained from Bio-Rad.

Immunoblotting analysis of TRIP13, p31^{comet} and MAD2 expression. For the data shown in **Supplementary Figure 7**, cell pellets were resuspended in lysis buffer (50 mM Tris pH 7.5, 150 mM NaCl and 0.5% NP-40 supplemented with one tablet per 10 ml of protease inhibitor cocktail (Roche) and 10 μM microcystin), vortexed and incubated for 20 min on ice. Lysates were clarified by centrifugation for 10 min and 4 °C at 14,000 rpm. Protein concentration was measured by Bradford assay using Coomassie Plus Proten Assay reagent (Thermo Scientific). Absorbance at 595 nm was measured on a spectrophotometer (Amersham). The primary antibodies used were to MAD2 (Bethyl, A300-301A), p31^{comet} (clone E29.19.14; a kind gift of A. Musacchio, MPI Dortmund), β-tubulin (Sigma, T4026) and TRIP13 (Bethyl, A303-605A). The secondary antibodies used were IRDye 800CW donkey anti-rabbit (926-32213) and IRDye 680CW donkey anti-mouse (926-68072). The molecular marker used was Odyssey One-Color Protein Molecular Weight Marker (928-40000). Quantitative immunoblotting was performed using an Odyssey infrared imager (LICOR Biosciences) running Odyssey v1.2 software. Images were opened in ImageStudio Lite, and mean intensity values were extracted by drawing rectangles around the bands of interest. The background was measured close to each individual band and automatically subtracted by the software. Protein levels were normalized to tubulin levels as a loading control.

Data availability. The authors declare that the data supporting the findings of this study are available within the paper and its supplementary information. The ICR1000 UK exome series data are available at the European Genome-phenome archive (EGA), reference number EGAD00001001021. Exome data for individual patients cannot be made publicly available for reasons of patient confidentiality. Qualified researchers may apply for access to these data, pending institutional review board approval.

22. Lunter, G. & Goodson, M. Stampy: a statistical algorithm for sensitive and fast mapping of Illumina sequence reads. *Genome Res.* **21**, 936–939 (2011).

23. Rimmer, A. *et al.* Integrating mapping-, assembly- and haplotype-based approaches for calling variants in clinical sequencing applications. *Nat. Genet.* **46**, 912–918 (2014).
24. Münz, M. *et al.* CSN and CAVA: variant annotation tools for rapid, robust next-generation sequencing analysis in the clinical setting. *Genome Med.* **7**, 76 (2015).
25. Abecasis, G.R. *et al.* An integrated map of genetic variation from 1,092 human genomes. *Nature* **491**, 56–65 (2012).
26. Gibson, D.G. *et al.* Enzymatic assembly of DNA molecules up to several hundred kilobases. *Nat. Methods* **6**, 343–345 (2009).
27. Drost, J. *et al.* Sequential cancer mutations in cultured human intestinal stem cells. *Nature* **521**, 43–47 (2015).
28. Carpenter, A.E. *et al.* CellProfiler: image analysis software for identifying and quantifying cell phenotypes. *Genome Biol.* **7**, R100 (2006).